Draft version November 9, 2024
Typeset using LaTeX default style in AASTeX631

Introducing the Condor Array Telescope. V. Deep Broad- and Narrow-Band Imaging Observations of the M81 Group

Kenneth M. Lanzetta,[1] Stefan Gromoll,[2] Michael M. Shara,[3] David Valls-Gabaud,[4] Frederick M. Walter,[1] and John K. Webb[5]

[1]*Department of Physics and Astronomy, Stony Brook University, Stony Brook, NY 11794-3800, USA*
[2]*Amazon Web Services, 410 Terry Ave. N, Seattle, WA 98109, USA*
[3]*Department of Astrophysics, American Museum of Natural History, Central Park West at 79th St., New York, NY 10024-5192, USA*
[4]*Observatoire de Paris, LERMA, CNRS, 61 Avenue de l'Observatoire, 75014 Paris, FRANCE*
[5]*Institute of Astronomy, University of Cambridge, Madingley Road, Cambridge CB3 0HA, UNITED KINGDOM*

(Received August 13, 2024)

Submitted to Astrophysical Journal Supplement

ABSTRACT

We used the Condor Array Telescope to obtain deep imaging observations through the luminance broad-band and He II 468.6 nm, [O III] 500.7 nm, He I 587.5 nm, Hα, [N II] 658.4 nm, and [S II] 671.6 nm narrow-band filters of an extended region comprising 13 "Condor fields" spanning $\approx 8 \times 8$ deg^2 on the sky centered near M81 and M82. Here we describe the acquisition and processing of these observations, which together constitute unique very deep imaging observations of a large portion of the M81 Group through a complement of broad- and narrow-band filters. The images are characterized by an intricate web of faint, diffuse, continuum produced by starlight scattered from Galactic cirrus, and all prominent cirrus features identified in the broad-band image can also be identified in the narrow-band images. We subtracted the luminance image from the narrow-band images to leave more or less only line emission in the difference images, and we masked regions of the resulting images around stars at an isophotal limit. The difference images exhibit extensive extended structures of ionized gas in the direction of the M81 Group, from known galaxies of the M81 Group, clouds of gas, filamentary structures, and apparent or possible bubbles or shells. Specifically, the difference images show a remarkable filament known as the "Ursa Major Arc;" a remarkable network of criss-crossed filaments between M81 and NGC 2976, some of which intersect and overlap the Ursa Major Arc; and details of a "giant shell of ionized gas."

Keywords: Galaxies (573), Galaxy groups (597), Galaxy interactions (600), Galaxy mergers (608), Galaxy photometry (611), Interacting galaxies (802), Low surface brightness galaxies (940), Galaxy tails (2125)

1. INTRODUCTION

The M81 Group consists of the galaxies M81, M82, NGC 3077, NGC 2976, and more than 30 other galaxies (Karachentsev 2005) that together stretch for more than 10 deg on the sky. The group is located just 3.6 Mpc away (Freedman et al. 1994), making it one of the nearest galaxy groups beyond the Local Group. The group is notable in that its most prominent members M81, M82, and NGC 3077 are strongly interacting, and this interaction has caused gas and stars to be stripped from the galaxies into a complex network of gaseous and stellar streams and has driven strong star-formation activity in the centers of M82 and NGC 3007. In fact, M82 is the prototypical and by far nearest example of a "starburst" galaxy with a high-velocity "superwind" that emanates from its center.

Analysis and interpretation of all deep imaging observations of the M81 Group are made complicated by two properties of the group: (1) The group exhibits a very low recession velocity, with M81 itself exhibiting a negative heliocentric recession velocity of -36 km s^{-1} (Kourkchi et al. 2020). This makes it difficult to distinguish features of Galactic origin from features at the distance of the group, even with spectroscopic observations in hand. And (2) the

group is located at a Galactic latitude of $b \approx 40$ deg in a direction of significant Galactic cirrus. Starlight scattered from the cirrus dominates the diffuse light seen in *both* broad- and narrow-band images, thereby muddying the view of foreground and background objects alike.

Over a period stretching from December 2021 through February 2024, we used the Condor Array Telescope (Lanzetta et al. 2023a) to obtain deep imaging observations through the luminance broad-band and He II 468.6 nm, [O III] 500.7 nm, He I 587.5 nm, Hα, [N II] 658.4 nm, and [S II] 671.6 nm narrow-band filters of an extended region comprising 13 "Condor fields"[1] spanning $\approx 8 \times 8$ deg^2 on the sky centered near M81 and M82. We obtained all broad-band observations at a cadence of one minute. Our motivation was severalfold:

- to characterize the Galactic cirrus in the direction of the M81 group to very sensitive levels;
- to search for ionized gas in the direction of the M81 Group, perhaps associated with the group or the cosmic web or perhaps associated with the Galaxy;
- to experiment with possibilities of combining deep imaging observations through both broad- and narrow-band filters to determine and subtract continuum from narrow-band images in regions of significant Galactic cirrus;
- to exploit the diagnostic capabilities of narrow-band images obtained through the [O III], Hα, [N II], and [S II] filters to determine or constrain physical properties of ionized gas;
- to use the broad-band observations obtained at a one-minute cadence to search for short-period planets transiting white dwarfs;
- to use the broad-band observations summed at a daily cadence to search for intergalactic novae in the outskirts of and between and around M81, M82, NGC 3077, NGC 2976, and other galaxies of the group;
- to use the broad- and narrow-band observations to search for intergalactic planetary nebulae in the outskirts of and between and around M81, M82, NGC 3077, NGC 2976, and other galaxies of the group;
- and to continue to establish and demonstrate the low-surface-brightness sensitivity of Condor through both broad- and narrow-band filters.

Here we describe the acquisition and processing of these observations, which we believe together constitute the deepest wide-field imaging observations of the M81 Group ever obtained through a complement of broad- and narrow-band filters. We use these observations to examine ionized gas in the direction of the M81 Group in Lanzetta et al. (2024), and we will present additional results of the analysis and interpretation of these observations elsewhere, addressing various of the topics noted above.

2. OBSERVATIONS

Condor is an "array telescope" that consists of six apochromatic refracting telescopes of objective diameter 180 mm, each equipped with a large-format (9576 × 6388 pixels), very low-read-noise (≈ 1.2 e$^-$), very rapid-read-time (< 1 s) CMOS camera. Details of the motivation, configuration, and performance of the telescope are described by Lanzetta et al. (2023a).

Over a period stretching from December 2021 through February 2024, we used Condor to obtain deep imaging observations through the luminance, He II 468.6 nm, [O III] 500.7 nm, He I 587.5 nm, Hα 656.3 nm, [N II] 658.4 nm, and [S II] 671.6 nm narrow-band filters of an extended region comprising 13 "Condor fields" spanning $\approx 8 \times 8$ deg^2 on the sky centered near M81 and M82. All exposures through the luminance filter were obtained with individual exposure times of 60 s, and all exposures through the narrow-band filters were obtained with individual exposure times of 600 s. The telescope was dithered by a random offset of ≈ 15 arcmin between each exposure.

Describing the resources devoted to a particular observation using an array telescope like Condor can be difficult in that the individual telescopes that comprise the array might be used in various filter configurations, with one or more telescopes allocated to a particular filter for a particular observation. (Further, various of the individual telescope might fail or be otherwise unavailable from time to time, temporarily taking them out of the mix.) To address this

[1] "Condor fields" are a set of fields with field centers that tile the entire sky with the Condor field of view, allowing for overlap.

issue, we introduce here the concept of the "reach" of an observation obtained by an array (or ordinary) telescope, which we define as the product of the total objective area and the total exposure time devoted to the observation. In its current configuration, Condor consists of six individual telescopes, each of objective diameter 180 mm or objective area 0.0254 m^2. Hence a one-second exposure with one telescope of the array yields a reach of 0.0254 m^2 s, and a one-second exposure with the entire array (i.e. with all six telescopes of the array) yields a reach of $6 \times 0.0254 = 0.153$ m^2 s. Because Condor is used with variety of filter configurations, with between one and six telescopes allocated to a particular filter for a particular observation, and because it is of interest to compare the capabilities of Condor with those of other telescopes, it is appropriate to employ the concept of the reach to concisely describe observations obtained using array telescopes.

Details of the observations are presented in Table 1, which for each pointing lists the Condor field identifier, the International Celestial Reference System (ICRS) J2000 coordinates of the field center, the filter, the start and end dates of the observations, and the reach as described above.

For comparison, the reach of narrow-band imaging observations of the galaxies M81 and M82 recently obtained by Lokhorst et al. (2022) using the Dragonfly Spectral Line pathfinder are 6.9×10^3 m^2 s through the Hα filter and 2.7×10^3 m^2 s through the [N II] 658.4 nm filter, over a field of view spanning 2×3 deg^2.

3. DATA PROCESSING

We processed the observations using the Condor data pipeline, which is described by Lanzetta et al. (2023a) and Lanzetta et al. (2023b). Briefly, the data pipeline performs bias subtraction; field flattening and background subtraction; astrometric calibration; identification and masking of cosmic ray events, satellite trails, and pixels that exhibit significant random telegraph noise; photometric calibration; drizzling onto a common coordinate grid; and coaddition of the individual exposures. After this processing, we combined the various groups of coadded images into mosaic images, yielding a total of seven mosaic images (one each obtained through the luminance and six narrow-band filters).

The resulting mosaic images obtained through the luminance and Hα filters are shown in Figures 1 and 2, as examples of the observations. All mosaic images (through the luminance, He II, [O III], He I, Hα, [N II], and [S II] filters) as well as all individual coadded images obtained through all filters are available for download on the Condor web site, as described in § 8 below. Each mosaic image contains $\approx 34,000 \times 34,000$ pixels (i.e. around a billion pixels) at a pixel scale of 0.85 arcsec pix^{-1}. Yet our primary interest here is on angular scales that are much larger than the angle subtended by a single pixel. Accordingly, the mosaic images are displayed here block averaged by 32×32 pixels, which yields an effective image size of $\approx 1000 \times 1000$ pixels at an effective pixel scale of 27.2 arcsec pix^{-1}.

We note several aspects of the mosaic images shown in Figures 1 and 2 and the other individual and mosaic coadded images as follows:

1. Because the reach varies between the individual coadded images (as presented in Table 1), the sensitivities of the mosaic images vary across the images. These variations are completely tracked by the uncertainty images associated with the individual coadded images that are produced by the data pipeline.

2. Due to technical difficulties with a filter wheel, there is a dearth of exposures obtained through the [S II] filter over the region covering roughly the left half of the mosaic image, and the exposures that were obtained over this region are of substandard quality. Although we present these data for the sake of completeness, we note that this region of the [S II] mosaic image should be excluded from any quantitative measurements.

3. A few very faint satellite trails survived the data processing, particularly in regions of images containing fewer than average exposures.

4. The images obtained through the He II and He I filters do not appear to show significant line emission.

The images shown in Figures 1 and 2 and the other mosaic and individual coadded images together constitute the deepest wide-field imaging observations of the M81 Group yet obtained through a complement of broad- and narrow-band filters. In terms of depth, angular resolution, and field of view, the luminance image provides an unprecedented view of the Galactic cirrus toward the M81 Group, while the narrow-band images provide an unprecedented view of ionized gas toward the M81 Group. The maximum 3σ surface-brightness sensitivity of the luminance image is 1.8×10^{-31} erg s^{-1} cm^{-2} Hz^{-1} $arcsec^{-2}$ over 10×10 $arcsec^2$ regions and 6.9×10^{-32} erg s^{-1} cm^{-2} Hz^{-1} $arcsec^{-2}$ over 32×32 pix^2 (or 27.2×27.2 $arcsec^2$) regions, and the maximum 3σ surface-brightness sensitivities of the narrow-band images regions are presented in Table 2 (recognizing that the sensitivities of the images vary across the images).

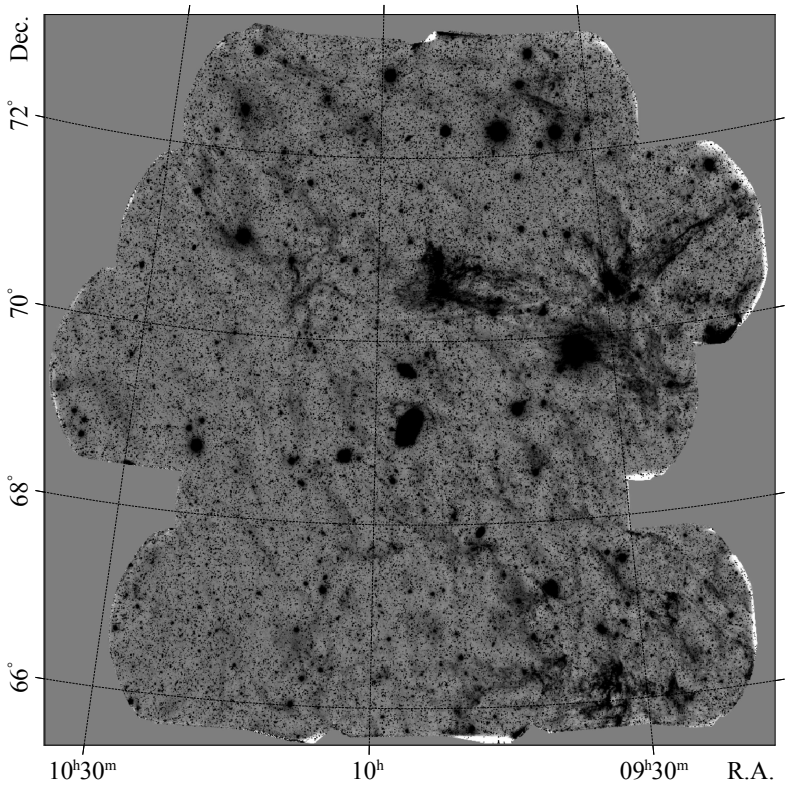

Figure 1. Mosaic image of M81 Group obtained through luminance filter. Image is displayed block averaged by 32×32 pixels.

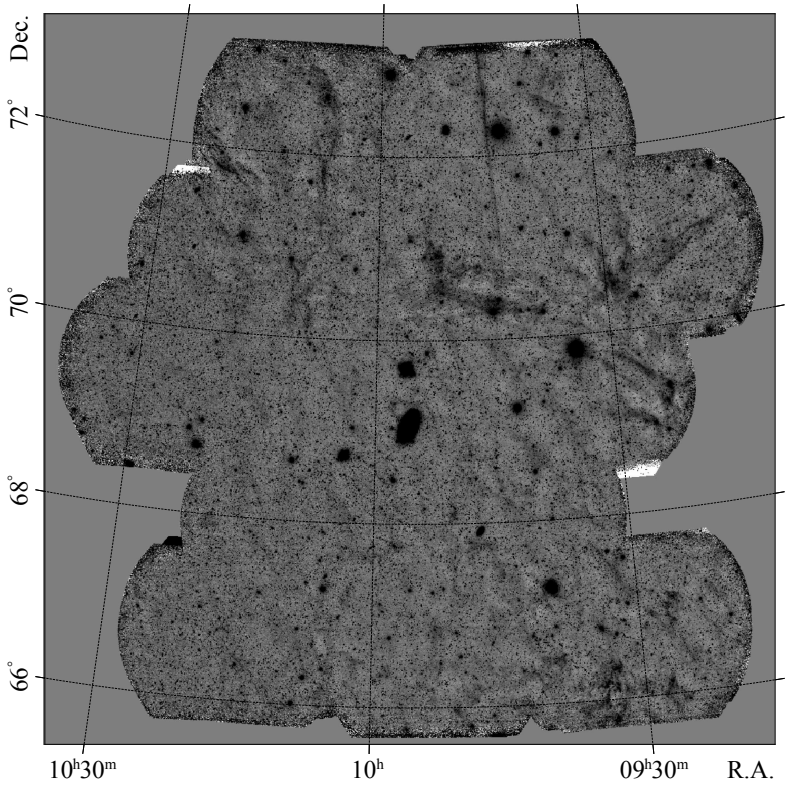

Figure 2. Mosaic image of M81 Group obtained through Hα filter. Image is displayed block averaged by 32×32 pixels.

Table 1: Details of Observations

	J2000			Start	End	Reach
Condor Field	R.A.	Dec	Filter	Date	Date	(m^2 s)
06917	09:25:42.86	+70:54:32.76	luminance	2021-11-30	2022-03-20	7,702.8
			He II 468.6 nm	2021-12-04	2022-03-16	519.1
			[O III] 500.7 nm	2021-12-04	2024-02-02	664.2
			He I 587.5 nm	2021-12-04	2022-03-16	351.2
			H-alpha 656.3 nm	2021-12-04	2024-02-02	790.1
			[N II] 658.4 nm	2021-12-04	2022-03-16	412.2
			[S II] 671.6 nm	2021-11-30	2024-02-02	224.4
06730	09:31:45.89	+66:49:05.52	luminance	2021-12-01	2022-03-25	7,737.9
			He II 468.6 nm	2021-12-04	2022-03-16	458.0
			[O III] 500.7 nm	2021-12-04	2024-01-07	618.4
			He I 587.5 nm	2021-12-04	2022-03-16	412.2
			H-alpha 656.3 nm	2021-12-04	2024-02-02	757.0
			[N II] 658.4 nm	2021-12-04	2023-04-28	488.6
			[S II] 671.6 nm	2021-12-04	2024-01-07	313.0
06859	09:36:00.00	+69:32:43.80	luminance	2021-11-30	2022-03-25	7,905.8
			He II 468.6 nm	2021-12-04	2022-03-16	503.8
			[O III] 500.7 nm	2021-12-04	2024-02-02	694.7
			He I 587.5 nm	2021-12-04	2022-03-16	488.6
			H-alpha 656.3 nm	2021-12-04	2024-02-01	806.7
			[N II] 658.4 nm	2021-12-04	2023-04-28	519.1
			[S II] 671.6 nm	2021-12-04	2024-02-01	267.2
06972	09:41:32.30	+72:16:21.72	luminance	2021-12-01	2022-03-25	6,562.2
			He II 468.6 nm	2021-12-04	2022-03-16	412.2
			[O III] 500.7 nm	2021-12-04	2024-01-07	572.6
			He I 587.5 nm	2021-12-04	2022-03-16	366.4
			H-alpha 656.3 nm	2021-12-04	2024-01-07	759.6
			[N II] 658.4 nm	2021-12-04	2023-04-28	442.8
			[S II] 671.6 nm	2021-12-04	2024-01-07	251.9
06797	09:45:00.00	+68:10:54.48	luminance	2021-11-30	2022-03-25	10,582.3
			He II 468.6 nm	2021-12-04	2022-03-16	320.6
			[O III] 500.7 nm	2021-12-04	2024-02-01	450.4
			He I 587.5 nm	2021-12-04	2022-03-16	366.4
			H-alpha 656.3 nm	2021-12-04	2024-02-01	713.8
			[N II] 658.4 nm	2021-12-04	2023-04-28	366.4
			[S II] 671.6 nm	2021-12-04	2024-02-01	221.4
06918	09:51:25.70	+70:54:32.76	luminance	2021-12-01	2022-03-25	8,825.0
			He II 468.6 nm	2021-12-04	2022-03-16	335.9
			[O III] 500.7 nm	2021-12-04	2024-02-01	482.2
			He I 587.5 nm	2021-12-04	2022-03-16	366.4
			H-alpha 656.3 nm	2021-12-04	2024-02-01	698.5
			[N II] 658.4 nm	2021-12-04	2023-04-28	335.9
			[S II] 671.6 nm	2021-12-04	2024-02-01	206.1
06731	09:52:56.47	+66:49:05.52	luminance	2021-11-30	2022-03-25	9,683.0
			He II 468.6 nm	2021-12-04	2022-03-16	335.9
			[O III] 500.7 nm	2021-12-04	2024-02-01	465.7
			He I 587.5 nm	2021-12-04	2022-03-16	351.2
			H-alpha 656.3 nm	2021-12-04	2024-02-01	606.9
			[N II] 658.4 nm	2021-12-04	2023-04-28	351.2
			[S II] 671.6 nm	2021-12-04	2024-02-01	161.6

Table 1 (continued)

Condor Field	J2000 R.A.	J2000 Dec	Filter	Start Date	End Date	Reach (m^2 s)
06860	10:00:00.00	+69:32:43.80	luminance	2021-12-01	2023-05-25	15,799.5
			He II 468.6 nm	2021-12-04	2023-02-27	1,710.0
			[O III] 500.7 nm	2021-12-04	2024-02-02	3,137.6
			He I 587.5 nm	2021-12-04	2023-02-27	1,786.4
			H-alpha 656.3 nm	2021-12-04	2024-02-04	622.2
			[N II] 658.4 nm	2021-12-04	2023-04-28	335.9
			[S II] 671.6 nm	2021-12-04	2024-02-04	160.3
06798	10:07:30.00	+68:10:54.48	luminance	2021-11-30	2022-03-25	8,246.3
			He II 468.6 nm	2021-12-04	2022-03-16	229.0
			[O III] 500.7 nm	2021-12-04	2024-01-01	271.0
			He I 587.5 nm	2021-12-04	2022-03-16	229.0
			H-alpha 656.3 nm	2021-12-04	2024-01-01	458.0
			[N II] 658.4 nm	2021-12-04	2023-04-28	244.3
			[S II] 671.6 nm	2021-12-04	2024-01-01	87.8
06973	10:09:13.85	+72:16:21.72	luminance	2021-12-01	2022-03-25	7,380.6
			He II 468.6 nm	2021-12-04	2022-03-16	244.3
			[O III] 500.7 nm	2021-12-04	2024-01-01	272.3
			He I 587.5 nm	2021-12-04	2022-03-16	259.6
			H-alpha 656.3 nm	2021-12-04	2024-01-01	459.3
			[N II] 658.4 nm	2021-12-04	2023-04-28	290.1
			[S II] 671.6 nm	2021-12-04	2024-01-01	87.8
06732	10:14:07.06	+66:49:05.52	luminance	2021-11-30	2022-03-25	7,473.7
			He II 468.6 nm	2021-12-04	2022-03-16	213.8
			[O III] 500.7 nm	2021-12-04	2024-01-01	255.7
			He I 587.5 nm	2021-12-04	2022-03-16	229.0
			H-alpha 656.3 nm	2021-12-04	2024-01-01	442.8
			[N II] 658.4 nm	2021-12-04	2023-04-28	229.0
			[S II] 671.6 nm	2021-12-04	2024-01-01	103.1
06919	10:17:08.57	+70:54:32.76	luminance	2021-12-03	2022-03-25	3,264.3
			He II 468.6 nm	2021-12-04	2022-03-16	183.2
			[O III] 500.7 nm	2021-12-04	2024-01-01	258.3
			He I 587.5 nm	2021-12-04	2022-03-16	106.9
			H-alpha 656.3 nm	2021-12-04	2024-01-01	398.2
			[N II] 658.4 nm	2021-12-04	2023-04-28	198.5
			[S II] 671.6 nm	2021-12-04	2024-01-01	87.8
06861	10:24:00.00	+69:32:43.80	luminance	2021-12-02	2022-03-25	6,078.2
			He II 468.6 nm	2021-12-04	2022-03-16	198.5
			[O III] 500.7 nm	2021-12-04	2024-01-01	286.3
			He I 587.5 nm	2021-12-04	2022-03-16	183.2
			H-alpha 656.3 nm	2021-12-04	2024-01-01	412.2
			[N II] 658.4 nm	2021-12-04	2023-04-28	213.8
			[S II] 671.6 nm	2021-12-04	2024-01-01	87.8

4. PHOTOMETRIC CALIBRATION

The Condor data pipeline uses measurements of continuum sources (i.e. stars) to determine photometric calibrations of all broad- and narrow-band images in terms of monochromatic energy flux densities (Lanzetta et al. 2023a,b). For measuring emission-line sources, it is more appropriate to express the calibration of the narrow-band images in terms

Table 2: Maximum Surface Brightness Sensitivities

	3σ sensitivity (10^{-18} erg s^{-1} cm^{-2} arcsec^{-2})	
Filter	10×10 arcsec^2	32×32 pix^2
He II 468.6 nm	3.0	1.1
[O III] 500.7 nm	6.6	2.4
He I 587.5 nm	2.1	0.78
Hα	3.9	1.4
[N II] 658.4 nm	9.6	3.6
[S II] 671.6 nm	11	3.9

of bolometric energy fluxes, integrated across the bandpasses of the filters. The [O III], Hα, [N II], and [S II] have bandpasses of FWHM $\approx$ 3 nm width, while the He II and He I filters have bandpasses of FWHM $\approx$ 4 nm width, and the response functions of all six narrow-band filters are characterized by very steep edges (Lanzetta et al. 2023a). Accordingly, we determined the photometric calibrations of the narrow-band images in terms of bolometric energy fluxes simply by multiplying the monochromatic energy flux densities by the nominal bandpasses of the filters. (The corresponding velocity widths of the filters are typically $\approx$ 1500 km s^{-1} for the narrower filters and $\approx$ 2000 km s^{-1} for the broader filters, i.e. much larger than the recession velocity of the M81 Group.)

To assess the accuracy of this procedure, we compared measurements of the bolometric energy fluxes of the Hα plus [N II] 658.4 nm emission lines of $\approx$ 500 H II regions in the outskirts of M81 between long-slit spectroscopy obtained by Lin et al. (2003) and the images obtained by Condor. (The energy fluxes of the emission lines were summed because the spectral resolution of the observations obtained by Lin et al. 2003 is insufficient to resolve Hα from [N II] 658.4 nm.) Results of the comparison are shown in Figure 3. It is evident from Figure 3 that the photometric calibrations of the Hα and [N II] images in terms of bolometric energy fluxes provide an excellent match to the spectroscopic observations, thereby demonstrating the accuracy of the calibrations.

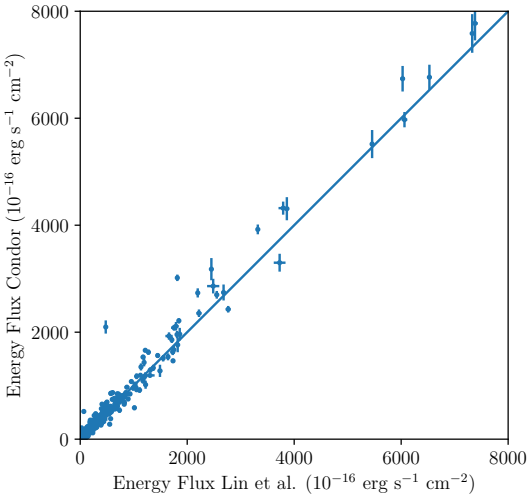

Figure 3. Comparison of measurements of bolometric energy fluxes of Hα plus [N II] 658.4 nm emission lines of $\approx$ 500 H II regions in outskirts of M81 between long-slit spectroscopy obtained by Lin et al. (2003) (horizontal axis) and images obtained by Condor (vertical axis). Line segment shows equal energy fluxes.

5. CONTINUUM SUBTRACTION

The most obvious and dramatic characteristic of the mosaic images obtained through *both* the luminance filter of Figure 1 and the Hα filter of Figure 2 is the intricate web of faint, diffuse, continuum produced by starlight scattered from Galactic cirrus. The surface brightness of the cirrus measured through the luminance filters spans the range $\approx$ 0.01 μJy arcsec^{-2} ($\approx$ 28.9 mag arcsec^{-2}) for the faintest detectable features through $\approx$ 0.4 μJy arcsec^{-2} ($\approx$ 24.9

mag arcsec^{-2}) for the brightest features. All prominent cirrus features identified in the luminance image can also be identified in the Hα image (and in the other narrow-band images). The cirrus is, of course, interesting in its own right, but here our primary objective is to search for ionized gas in the direction of the M81 Group, and toward this end, it is a nuisance.

Indeed one of our motivations for targeting the M81 Group was to experiment with possibilities of combining deep imaging observations through both broad- and narrow-band filters to determine and subtract continuum from narrow-band images in regions of significant Galactic cirrus. The cirrus is a near-universal obstacle that all low-surface-brightness imaging observations—broad- or narrow-band imaging observations of extragalactic or Galactic objects—must contend with, and it is often the most significant source of systematic uncertainty associated with deep imaging observations. Hence it is clearly of interest to find a way to account for the cirrus.

All of the mosaic images are expressed on a common coordinate grid and are characterized by similar (although not identical) point-spread functions. And to at least a first approximation, any line emission is insignificant in comparison to continuum over the very large bandpass of the luminance filter, so the luminance image roughly traces continuum, whereas the narrow-band images trace line emission plus continuum. Hence we expect that subtracting the luminance image from the narrow-band images should leave more or less only line emission in the difference images.

But this is true only to the extent that the continuum is achromatic. Because the luminance and narrow-band images are nominally calibrated in AB magnitudes (Oke & Gunn 1983), "achromatic" in this context means of flat specific energy flux per unit frequency interval f_ν. This is clearly *not* the case for stars, so we should not expect this procedure to account for stars perfectly. And depending on the color of the cirrus and the wavelength centroid of some narrow-band filter with respect to the luminance filter, it might be necessary to scale the luminance image by some factor of order unity to account for the cirrus properly.

With this in mind, we subtracted continuum from each narrow-band image according to the following procedure: First, we subtracted the luminance image from the narrow-band image to form the difference image. Next, we masked regions of the difference image around stars contained in the Gaia DR3 catalog (Gaia Collaboration et al. 2017, 2018, 2021; Gaia Collaboration 2022) at an isophotal limit, replacing the values of the masked pixels with the value of the median of nearby pixels. (This procedure leaves the imprints of faint stars below the limit of Gaia, which we did not attempt to remove in order to assure that we did not inadvertently remove bona fide sources of line emission.) Finally, we repeated this procedure after scaling the luminance image by a factor of order unity in order to best account for and remove the cirrus. This last step is clearly subjective, but we found through experimentation that it is possible to determine a scale that accounts for and removes essentially all of the cirrus.

The resulting mosaic difference images obtained through the [O III], Hα [N II], and [S II] filters are shown in Figures 4 through 7, again displayed block averaged by 32×32 pixels. All mosaic difference images (through the He II, [O III], He I, Hα, [N II], and [S II] filters) are available for download on the Condor web site, as described in § 8 below.

Comparing the mosaic difference images of Figures 4 through 7 with the mosaic image obtained through the luminance filter shown in Figure 1, it is evident that the continuum subtraction procedure performed exceptionally well. The mosaic difference images show little evidence of residual continuum except possibly for a very few isolated features. We conclude that even very substantial continuum contributed by Galactic cirrus over a very large field of view can be subtracted to high accuracy given a sufficiently high quality luminance image to characterize the cirrus; accounting for color variations of the cirrus (by using images obtained through multiple broad-band filters rather than only the luminance filter) would likely do better still.

6. AN OVERVIEW OF IONIZED GAS IN THE DIRECTION OF THE M81 GROUP

The mosaic difference images of Figures 4 through 7 exhibit extensive extended structures of ionized gas in the direction of the M81 Group. Emission from these structures is particularly prominent in Hα and [N II], although emission from some portions of some of these structures is also evident in [O III] and [S II]. In general, the emission exhibits a complex patchy and filamentary nature, and it is not at all obvious how to distinguish emission associated with the M81 Group from emission associated with the Galaxy. (And neither is is obvious how spectroscopic observations would resolve this ambiguity, given the low recession velocity of the group.) Here we present a brief overview of ionized gas in the direction of the M81 Group, describing some of the more prominent features visible in the images and trying as best we can to group features that appear to be related based on location and morphology.

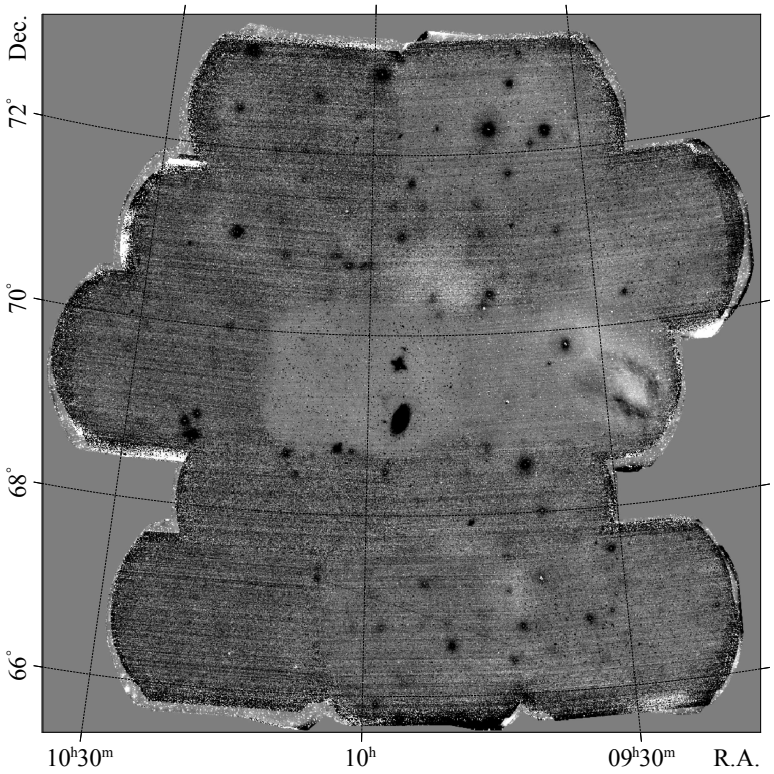

Figure 4. Mosaic difference image of M81 Group obtained through [O III] filter formed by subtracting luminance image from [O III] image and masking known stars. Image is displayed block averaged by 32×32 pixels.

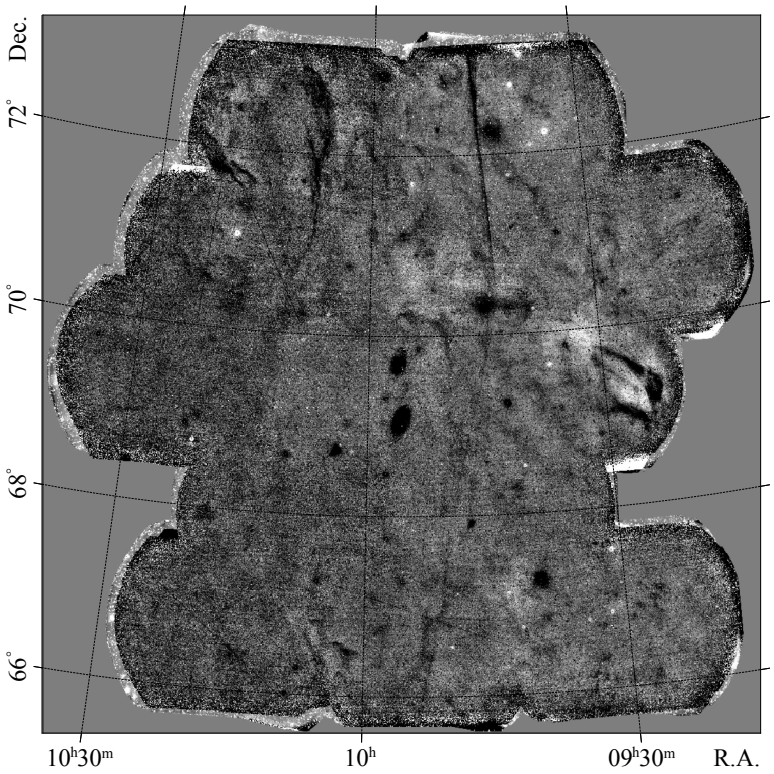

Figure 5. Mosaic difference image of M81 Group obtained through Hα filter formed by subtracting luminance image from Hα image and masking known stars. Image is displayed block averaged by 32×32 pixels.

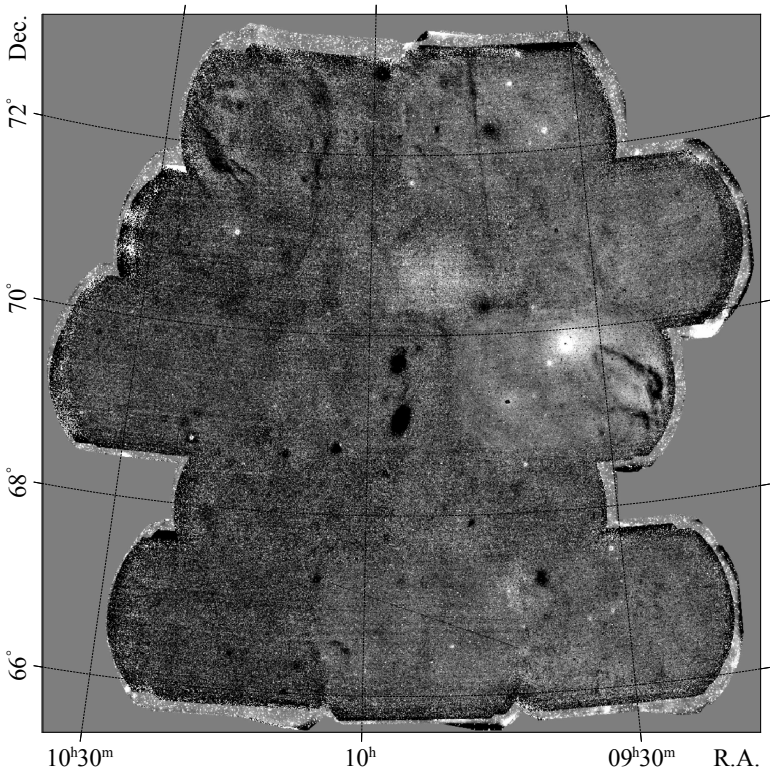

Figure 6. Mosaic difference image of M81 Group obtained through [N II] filter formed by subtracting luminance image from [N II] image and masking known stars. Image is displayed block averaged by 32×32 pixels.

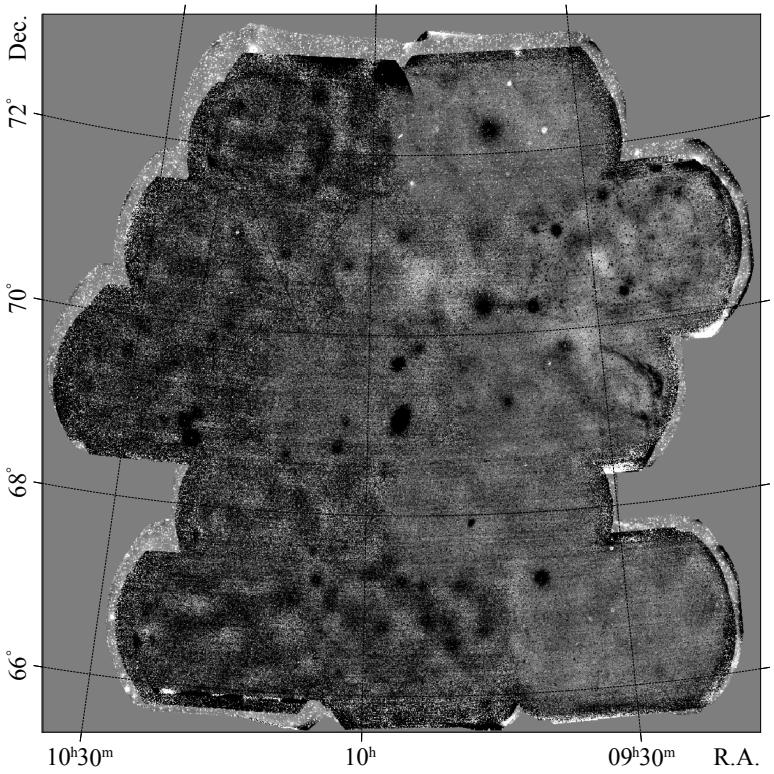

Figure 7. Mosaic difference image of M81 Group obtained through [S II] filter formed by subtracting luminance image from [S II] image and masking known stars. Image is displayed block averaged by 32×32 pixels.

6.1. *Schematic Depiction*

A schematic depiction of some of the extended structures of ionized gas in the direction of the M81 Group is shown in Figure 8 overlaid upon the Hα mosaic difference image. Specifically, Figure 8 attempts to depict (1) known galaxies of the M81 Group (shown as shaded light green circles or ovals), (2) clouds of gas (shown as shaded light blue circles, ovals, or irregular shapes), (3) filamentary (or essentially one-dimensional) structures (shown as pink curves or shaded pink shapes), and (4) apparent or possible bubbles or shells (shown as open yellow circles) and to exclude known stars and known galaxies not of the M81 Group. The features depicted in Figure 8 were drawn by hand, attempting as best as possible to group objects that appear to be related. Figure 8 designates some, but not all, of the depicted features or groups of features with a letter designation. Figure 8 is not intended to definitively or exhaustively catalog the ionized gas in the direction of the M81 Group but rather is intended only to introduce the shapes, sizes, and locations of some of the extended structures of ionized gas in the direction of the M81 in order that these structures can be referred to subsequently. In the following sections, we call attention to some of the particularly striking and remarkable features shown in Figure 8; we will present results of the analysis and interpretation of these observations elsewhere.

6.2. *Galaxies of the M81 Group*

Eight known galaxies of the M81 Group are visible in one or more of the mosaic difference images. Details of these galaxies are presented in Table 3, which for each galaxy lists the galaxy name, designation in Figure 8, and ICRS J2000 coordinates. There are other galaxies of the M81 Group that are not visible in the mosaic difference images, and there are other galaxies not of the M81 Group that are visible in the mosaic difference images.

Table 3: Details of Galaxies Visible in Images

		J2000	
Galaxy	Designation	R.A.	Dec
M81	A	09:55:33.2	+69:03:55.1
M82	B	09:55:52.4	+69:40:46.9
NGC 3077	C	10:03:19.1	+68:44:01.6
NGC 2976	D	09:47:15.5	+67:54:59.0
UGC 5139	E	09:40:32.3	+71:10:56.0
UGC 5692	F	10:30:35.0	+70:37:07.2
HIJASS J1021+68	G	10:21:00.2	+68:42:00.0
IC 2574	H	10:28:23.6	+68:24:43.4
UGC 5536	I	09:57:32.9	+69:02:50.7

6.3. *Ursa Major Arc*

The mosaic difference images show a remarkable filament known as the "Ursa Major Arc" (McCullough & Benjamin 2001; Bracco et al. 2020) that runs roughly N-S across the entire field of view. The filament is visible in the Hα and [N II] mosaic difference images. The filament is designated in Figure 8 as comprised of two pieces: a northern piece that runs between filament designations A and B, and a southern piece that runs between filament designations C and D. The character of the filament changes across the Hα and [N II] images in the sense that it appears thicker toward the N and thinner toward the S, and the filament appears to exhibit a discontinuity coincident with cloud J. The Ursa Major Arc is known to stretch ≈ 30 deg on the sky (Bracco et al. 2020) and has been interpreted variously as a trail of ionized gas produced by an unseen ionizing source (McCullough & Benjamin 2001) and as an interstellar shock (Bracco et al. 2020). It is notable that the Ursa Major Arc passes within only ≈ 0.75 deg of the center of M81.

6.4. *Additional Filaments*

The mosaic difference images show a remarkable network of criss-croseds filaments, some of which intersect and overlap the Ursa Major Arc. The filaments are visible in the Hα mosaic difference image, and some of the filaments are visible in the [N II] mosaic difference image. The epicenter of the network of filaments appears to be located ≈ 0.9 deg SW of M81, between M81 and NGC 2976. The filaments are too numerous to cleanly designate individually in Figure 8, so only some of the filaments are designated. At least three of the filaments appear to originate or terminate

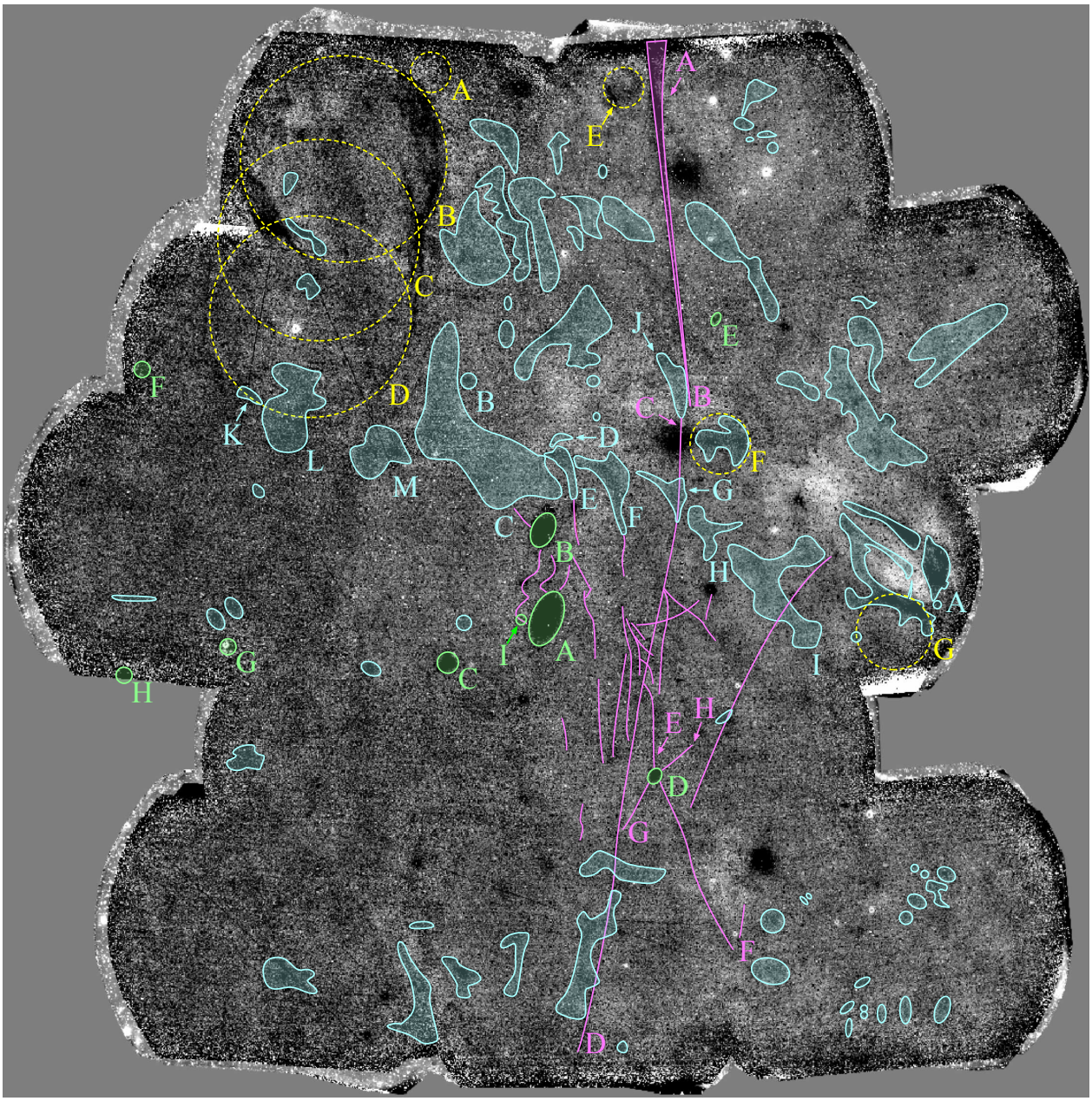

Figure 8. Schematic depiction of ionized gas in direction of M81 Group. Known galaxies of M81 Group are shown as shaded light green circles or ovals), clouds of gas are shown as shaded light blue circles, ovals, or irregular shapes, filamentary (or essentially one-dimensional) structures are shown as pink curves or shaded pink shapes, and apparent or possible bubbles or shells are shown as open yellow circles. Known stars and known galaxies not of M81 Group are not indicated. Letter designations are positioned to lower right of corresponding features unless otherwise noted by arrow. Figure is not intended to definitively or exhaustively catalog ionized gas in direction of M81 Group but rather is intended only to introduce shapes, sizes, and locations of some of extended structures of ionized gas in direction of M81 in order that these structures can be referred to subsequently.

on NGC 2976: one at roughly 12 o'clock (designated filament E), one at roughly 5 o'clock (filament F), and one at roughly 7 o'clock (filament G). Filaments E and G (as well as some of the undesignated filaments) appear to intersect and overlap the Ursa Major Arc.

6.5. *Giant Shell of Ionized Gas*

The mosaic difference images show the "giant shell of ionized gas" discovered by Lokhorst et al. (2022) located ≈ 0.6 deg to the NW of M82. The giant shell is visible in the Hα and [N II] mosaic difference images. These mosaic difference images reveal several new aspects of the giant shell:

1. The giant shell is clearly comprised of at least two pieces; an eastern piece designated in Figure 8 as cloud E, and a western piece designated as cloud F. The western-most edge of cloud F is located within ≈ 0.35 deg of the Ursa Major Arc.

2. Both pieces of the giant shell exhibit similar morphologies, with a shape that resembles a "comma." Further, both pieces appear to extend toward the S in thin filaments. These filaments form part of the network of criss-crossed filaments that intersect and overlap the Ursa Major Arc described above.

3. There is another cloud designated as cloud G located immediately to the W of cloud F that exhibits a morphology similar to those of clouds E and F, with a shape that also resembles a comma. Cloud G is essentially coincident with the Ursa Major Arc.

4. In fact, clouds E, F, and G appear to form part of a larger chain of clouds that run roughly NE to SW that includes clouds designated as clouds K, L, M, B, C, and D to the E and clouds H and I to the W. It is, of course, uncertain whether these clouds are physically related or even at the same distance.

6.6. *Vicinity of M81 and M82*

The mosaic difference images show various features in the vicinity of M81 and M82, including the well-known "Hα cap" of M82 (Devine & Bally 1999; Lehnert et al. 1999) located ≈ 9 arcmin NW of the center of M82, the "Hα ridge" discovered by Lokhorst et al. (2022) located roughly midway between the outer extent of M82 and the Hα cap, and the "Hα-emitting filament" the "Hα-emitting clump" noted previously by Pasha et al. (2021). The features are visible in the Hα mosaic difference image, and some of the features are visible in the [O III], [N II], and [S II] mosaic difference images. Some of the features cannot be resolved from M82 in the mosaic difference images shown in Figures 4 through 7 but are easily visible on the images displayed block averaged on a finer scale.

6.7. *Rattlesnake Head Nebula*

The mosaic difference images show an apparent emission nebula located near the western edge of the field of view, due almost exactly W of the midpoint between M81 and M82. The nebula is visible in all four of the mosaic difference images. The nebula appears to be comprised of several distinct pieces, which are collectively designated in Figure 8 as cloud A. The shape of the nebula reminds us of the head of a rattlesnake, and we dub the nebula the "Rattlesnake Head Nebula."

6.8. *Apparent or Possible Bubbles or Shells*

The mosaic difference images show several apparent or possible bubbles or shells. The bubbles or shells are visible in the Hα mosaic difference image, and some of the bubbles or shells are visible in the [N II] mosaic difference image. A particularly striking apparent bubble or shell designated in Figure 8 as bubble B comprises two near halves of nearly-circular feature in the upper-left corner of the image, with a center due NE of M81 and M82 and a radius of ≈ 0.75 deg. A second particularly striking apparent bubble or shell designated as bubble D is located due S of bubble B, also with a radius of ≈ 0.75 deg. A possible piece of a bubble or shell designated as bubble C is located between bubbles B and D. A possible bubble or shell designated as bubble F is located near the discontinuity of the Ursa Major Arc coincident with cloud J, with a radius of ≈ 0.2 deg. And a possible bubble or shell designated as bubble G is located just S of the Rattlesnake Head Nebula. Other possible bubbles or shells designated as A and E are located N of M81 and M82.

6.9. *Other Emission Features*

The mosaic difference images show a large number of other emission features, of a variety of sizes, shapes, and brightnesses. Although we do not individually enumerate all of these other features here, they can be picked out in the mosaic difference images of Figures 4 through 7 or in the images available for download on the Condor web site, as described in § 8 below. The various emission features visible in the mosaic difference images could be targets of future spectroscopic observations with large ground-based telescopes, although as noted above, the very low recession velocity of the M81 Group will make it difficult to distinguish features of Galactic origin from features at the distance of the group.

7. SUMMARY

We used the Condor Array Telescope to obtain deep imaging observations through the luminance broad-band and He II 468.6 nm, [O III] 500.7 nm, He I 587.5 nm, Hα, [N II] 658.4 nm, and [S II] 671.6 nm narrow-band filters of an extended region comprising 13 "Condor fields" spanning $\approx 8 \times 8$ deg^2 on the sky centered near M81 and M82. Here we describe the acquisition and processing of these observations, which together constitute unique very deep imaging observations of a large portion of the M81 Group through a complement of broad- and narrow-band filters. The images obtained through the broad-band filter and the narrow-band filters are characterized by an intricate web of faint, diffuse, continuum produced by starlight scattered from Galactic cirrus, and all prominent cirrus features identified in the broad-band image can also be identified in the narrow-band images. We subtracted the luminance image from the narrow-band images to leave more or less only line emission in the difference images, and we masked regions of the resulting images around stars at an isophotal limit.

The mosaic difference images exhibit extensive extended structures of ionized gas in the direction of the M81 Group, from known galaxies of the M81 Group, clouds of gas, filamentary structures, and apparent or possible bubbles or shells. Specifically, the difference images show a remarkable filament known as the "Ursa Major Arc;" a remarkable network of criss-crossed filaments between M81 and NGC 2976, some of which intersect and overlap the Ursa Major Arc; details of a "giant shell of ionized gas;" and a large number of other emission features.

8. DATA AVAILABILITY

All raw Condor data are available following an 18-month proprietary period. All raw and processed data described here, including the coadded mosaic images of and the mosaic difference images, are available on the Condor web site https://condorarraytelescope.org/data_access/ or by contacting the corresponding author.

This material is based upon work supported by the National Science Foundation under Grants 1910001, 2107954, 2108234, 2407763, and 2407764. We gratefully acknowledge the staff of Dark Sky New Mexico, including Diana Hensley and Michael Hensley for their superb logistical and technical support. The authors thank the anonymous referee for very valuable comments.

Software: astroalign (Beroiz et al. 2020), astropy (Astropy Collaboration et al. 2013, 2018), django (Django Software Foundation 2019), Docker (Merkel 2014), DrizzlePac (Gonzaga et al. 2012), NoiseChisel (Akhlaghi & Ichikawa 2015; Akhlaghi 2019), numba (Lam et al. 2015), numpy (Harris et al. 2020), photutils (Bradley et al. 2020), scipy (Virtanen et al. 2020), SExtractor (Bertin & Arnouts 1996)

REFERENCES

Akhlaghi, M. 2019, arXiv e-prints, arXiv:1909.11230. https://arxiv.org/abs/1909.11230

Akhlaghi, M., & Ichikawa, T. 2015, ApJS, 220, 1, doi: 10.1088/0067-0049/220/1/1

Astropy Collaboration, Robitaille, T. P., Tollerud, E. J., et al. 2013, A&A, 558, A33, doi: 10.1051/0004-6361/201322068

Astropy Collaboration, Price-Whelan, A. M., Sipőcz, B. M., et al. 2018, AJ, 156, 123, doi: 10.3847/1538-3881/aabc4f

Beroiz, M., Cabral, J., & Sanchez, B. 2020, Astronomy and Computing, 32, 100384, doi: https://doi.org/10.1016/j.ascom.2020.100384

Bertin, E., & Arnouts, S. 1996, A&AS, 117, 393, doi: 10.1051/aas:1996164

Bracco, A., Benjamin, R. A., Alves, M. I. R., et al. 2020, A&A, 636, L8, doi: 10.1051/0004-6361/202037975

Bradley, L., Sipőcz, B., Robitaille, T., et al. 2020, astropy/photutils: 1.0.0, 1.0.0, Zenodo, doi: 10.5281/zenodo.4044744

Devine, D., & Bally, J. 1999, ApJ, 510, 197, doi: 10.1086/306582

Django Software Foundation. 2019, Django, 2.2.1. https://djangoproject.com

Freedman, W. L., Hughes, S. M., Madore, B. F., et al. 1994, ApJ, 427, 628, doi: 10.1086/174172

Gaia Collaboration. 2022, VizieR Online Data Catalog, I/355

Gaia Collaboration, Clementini, G., Eyer, L., et al. 2017, A&A, 605, A79, doi: 10.1051/0004-6361/201629925

Gaia Collaboration, Brown, A. G. A., Vallenari, A., et al. 2018, A&A, 616, A1, doi: 10.1051/0004-6361/201833051

—. 2021, A&A, 649, A1, doi: 10.1051/0004-6361/202039657

Gonzaga, S., Hack, W., Fruchter, A., & Mack, J. e. 2012, The DrizzlePac Handbook, STScI, Baltimore, MD

Harris, C. R., Millman, K. J., van der Walt, S. J., et al. 2020, Nature, 585, 357, doi: 10.1038/s41586-020-2649-2

Karachentsev, I. D. 2005, AJ, 129, 178, doi: 10.1086/426368

Kourkchi, E., Tully, R. B., Eftekharzadeh, S., et al. 2020, ApJ, 902, 145, doi: 10.3847/1538-4357/abb66b

Lam, S. K., Pitrou, A., & Seibert, S. 2015, in Proceedings of the Second Workshop on the LLVM Compiler Infrastructure in HPC, 1–6

Lanzetta, K. M., Gromoll, S., Shara, M. M., et al. 2023a, PASP, 135, 015002, doi: 10.1088/1538-3873/acaee6

—. 2024, ApJL

—. 2023b, MNRAS

Lehnert, M. D., Heckman, T. M., & Weaver, K. A. 1999, ApJ, 523, 575, doi: 10.1086/307762

Lin, W., Zhou, X., Burstein, D., et al. 2003, The Astronomical Journal, 126, 1286, doi: 10.1086/377519

Lokhorst, D., Abraham, R., Pasha, I., et al. 2022, ApJ, 927, 136, doi: 10.3847/1538-4357/ac50b6

McCullough, P. R., & Benjamin, R. A. 2001, AJ, 122, 1500, doi: 10.1086/322097

Merkel, D. 2014, Linux journal, 2014, 2

Oke, J. B., & Gunn, J. E. 1983, ApJ, 266, 713, doi: 10.1086/160817

Pasha, I., Lokhorst, D., van Dokkum, P. G., et al. 2021, ApJL, 923, L21, doi: 10.3847/2041-8213/ac3ca6

Virtanen, P., Gommers, R., Oliphant, T. E., et al. 2020, Nature Methods, 17, 261, doi: 10.1038/s41592-019-0686-2